THE SMALL-SCALE STRUCTURE OF ACCELERATION IN TURBULENT CHANNEL FLOW

Kenneth T. Christensen and Ronald J. Adrian
Laboratory for Turbulence and Complex Flow
Department of Theoretical and Applied Mechanics
University of Illinois at Urbana-Champaign
Urbana, IL 61801 USA
kchrstns@uiuc.edu and r-adrian@uiuc.edu

ABSTRACT

Temporal and convective derivatives of velocity are computed from time-resolved particle-image velocimetry data in the streamwise–wall-normal plane of turbulent channel flow. Advection of the small-scale vortices embedded within the flow dominates the small-scale behavior of the velocity time-derivative; however, in a reference frame traveling with the vortices, a marked deceleration represents the evolution of the flow. This large-scale deceleration is conjectured to be the dynamic influence of larger-scale vortices present further away from the wall on the smaller-scale vortices present closer to the wall.

INTRODUCTION

The Navier–Stokes equation

$$\frac{\partial u_i}{\partial t} = -u_j \frac{\partial u_i}{\partial x_j} - \frac{1}{\rho}\frac{\partial p}{\partial x_i} + \nu \frac{\partial^2 u_i}{\partial x_j \partial x_j}, \quad (1)$$

relates the local rate of change of the flow to the advective, pressure, and viscous effects of the flow, respectively, on the right-hand side of (1). While $\partial u_i/\partial t$ represents the local rate of change of the flow in a fixed reference frame, the fluid particle acceleration is given by the material derivative of velocity:

$$\frac{\mathrm{D} u_i}{\mathrm{D} t} \equiv \frac{\partial u_i}{\partial t} + u_j \frac{\partial u_i}{\partial x_j}. \quad (2)$$

Therefore, the material derivative of velocity embodies the pressure and viscous accelerations imposed by the flow, the mechanisms that influence its evolution. Although $\partial u_i/\partial t$ embodies the same evolution mechanisms, their influence is often masked by the more dominant advection of the small scales. The evolution of the flow in a fixed reference frame can be assessed by replacing u_j in (2) with a constant convection velocity, yielding a bulk or mean convective derivative.

Characterizing the evolution of the flow (from both the statistical and structural viewpoint) is necessary for extending optimal formulations of large-eddy simulation (LES) sub-grid scale modeling to higher Reynolds numbers. Optimal formulations are based upon minimizing the mean-square error associated with estimating the short-term dynamics of the resolved (large) scales. This error is minimized when

$$\frac{\partial \tilde{u}_i}{\partial t} = \left\langle \frac{\partial \tilde{u}_i}{\partial t} \middle| \tilde{\mathbf{u}} \right\rangle, \quad (3)$$

where $(\tilde{\ })$ represents a filtering operation that defines the boundary between the resolved and modeled scales of the flow. Defining this boundary is one of the key elements in LES, especially for proper *structural* modeling of the sub-grid scales.

The statistical behavior of the temporal and material derivatives of velocity has been studied in the context of scalar transport (Yueng, 1997; Hill and Thoroddsen, 1997; Pinsky et al., 2000, for example). However, the relationship between dominant vortical structures and acceleration has not been investigated heretofore. In this paper, dominant temporal- and convective-derivative events are studied in relation to the vortical structures commonly found in wall turbulence. This comparison is essential for proper structure modeling of wall turbulence in the context of optimal formulations for LES sub-grid scale modeling because any distinct small-scale and large-scale dynamic behavior can physically motivate the selection of a suitable boundary between the resolved and modeled scales.

EXPERIMENT

The experiments which form the basis of this work are performed in turbulent channel

flow. The working fluid is air and the facility is driven by a centrifugal blower. The apparatus has a channel cross-section of 5.08 cm × 51.44 cm ($2h$ × width, where h is the half-height of the channel) and has a development length of $216h$. Particle-image velocimetry (PIV) is used to measure two-dimensional velocity (u,v) fields in the streamwise–wall-normal (x–y) plane along the channel centerline separated by a small time delay, facilitating the calculation of the temporal derivative of velocity. The measurement domain is $h \times h$, and 875 statistically independent pairs of velocity realizations are acquired at $\mathrm{Re}_\tau = u_\tau h/\nu = 547$ and 1734.

At high Reynolds numbers, it is difficult to adequately resolve the temporal evolution of the flow with standard PIV imaging equipment, primarily due to the limited framing rates of current CCD cameras. Standard cross-correlation cameras used for PIV have a typical frame rate of 30 Hz. At high Re, the flow would advect completely out of the field of view during this time, making time-derivative calculations impossible. Therefore, current imaging technology must be exploited in a more novel manner to allow time-resolved PIV measurements for time delays much smaller than the camera frame rates.

With the above constraint in mind, a two-CCD-camera arrangement is used in this research to measure channel-flow velocity fields separated by very small time delays, on the order of microseconds. Specifically, a separate PIV measurement is made with each CCD camera, such that the second measurement occurs slightly later in time relative to the first (the cameras are focused upon identical flow domains). Since the repetition rate of Nd:YAG lasers is slow compared to the dynamics of the flow, the field of view is illuminated by two pairs of Nd:YAG lasers which, in concert, produce four distinct laser pulses (two pulses per CCD camera, each pair offset in time). An added complication arises since the shutter times of the CCD cameras are an order of magnitude larger than the time delays considered in this research. Therefore, the particle images meant to be viewed by only one CCD camera must not reach the other CCD camera. Fortunately, since the seed particles used in this experiment are quite small ($\sim 1\mu$m), light scattered from these particles maintains the properties of the incident light. *Specifically, the scattered light from particles of this size maintains the polarization of the incident light* (Adrian and Earley, 1976). With this
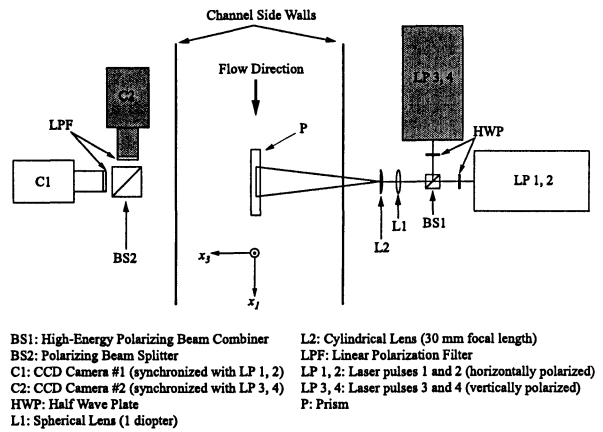

Figure 1: Experimental setup, viewed from above. Shading of lasers and cameras indicates which laser pulses are synchronized with which camera.

BS1: High-Energy Polarizing Beam Combiner
BS2: Polarizing Beam Splitter
C1: CCD Camera #1 (synchronized with LP 1, 2)
C2: CCD Camera #2 (synchronized with LP 3, 4)
HWP: Half Wave Plate
L1: Spherical Lens (1 diopter)
L2: Cylindrical Lens (30 mm focal length)
LPF: Linear Polarization Filter
LP 1, 2: Laser pulses 1 and 2 (horizontally polarized)
LP 3, 4: Laser pulses 3 and 4 (vertically polarized)
P: Prism

in mind, the particle images viewed by each camera are *coded* by polarizing the incident light in a predetermined manner. This filtering methodology is explained in greater detail below in the context of the actual measurement system. We refer to this collective experimental methodology as particle-image accelerometry.

Figure 1 illustrates the optical setup used in this experiment. Four Nd:YAG lasers (New Wave Research Gemini series) are used as illumination sources. These lasers emit 120 mJ/pulse at a repetition rate of 15 Hz and have a pulse width of 6 ns. The first two pulses provide illumination for the first camera (laser and camera are shaded white in Figure 1), while the second two laser pulses illuminate the field of view for the second camera (lasers and camera are shaded gray). The second two laser pulses and the second camera are delayed in time by τ using a digital-delay generator, such that the second camera views the flow at a slightly later time than the first. In order to distinguish between the sets of pulses, the first two pulses (LP 1,2) are rotated to horizontal polarization, while the second two pulses (LP 3,4) are rotated to vertical polarization with half wave plates (HWP). All laser pulses are then combined along a common optical path with a polarization beam splitter acting as a beam combiner (BS1). The horizontally polarized light from LP 1,2 passes through the beam splitter, while the vertically-polarized light from LP 3,4 is reflected onto the optical path. All pulses then follow the same optical path: through a standard spherical lens (L1) and then through a standard cylindrical lens (L2). The resulting light sheets are deflected 90° with a right-angle prism (P) from the x_1–x_3 plane into the x_1–x_2 plane along the

22

centerline of the test section.

The scattered light from the seed particles is imaged onto one of the two CCD cameras depending on the polarization of the light. A polarizing beam splitter (BS2) guides each polarization to the appropriate camera. The horizontally polarized scattered light is transmitted through the beam splitter and imaged by the first CCD camera (C1), while the vertically polarized light is reflected by the beam splitter and imaged by the second CCD camera (C2).

INSTANTANEOUS TEMPORAL AND CONVECTIVE DERIVATIVE FIELDS

Figure 2(a) is an instantaneous velocity realization in the streamwise–wall-normal plane of the channel at $Re_\tau = 547$. A constant advection velocity has been removed to visualize the vortices that are advecting at this speed. Two vortex cores are visible in the velocity field, each circled to accentuate its spatial extent. These vortices are thought to be the heads of hairpin/hairpin-like vortices propagating as coherent groups in the streamwise direction. The groups, referred to as *hairpin vortex packets*, can contain as many as 10 vortices and extend to nearly twice the outer length scale in the streamwise direction (Adrian et al., 2000).

The field of the local rate of change of the velocity shown in Figure 2(a) is presented in Figure 2(b). A simple first-order, forward-differencing scheme is used to calculate the temporal derivatives of velocity, yielding

$$\frac{\partial u_i}{\partial t}(\mathbf{x}, t) \approx \frac{u_i^{C2}(\mathbf{x}, t + \tau) - u_i^{C1}(\mathbf{x}, t)}{\tau}, \quad (4)$$

where C1 and C2 refer to the velocity fields measured by cameras 1 and 2, respectively. The circles of Figure 2(a) are replicated in the $\partial u_i/\partial t$ field in order to aid in associating dominant velocity time-derivative patterns with the vortices themselves. A clear velocity time-derivative "signature" is associated with each vortex and consists of a strong wall-normal acceleration near the center of each vortex, coupled with a weak streamwise deceleration at the same location. In addition, a rotational pattern exists within the velocity time-derivative field outboard of the strong wall-normal acceleration region on both sides. Thus, the complete rate of change "signature" associated with each vortex appears to be a mushroom-like pattern.

In contrast, the mushroom-like pattern is absent in the bulk convective-derivative field
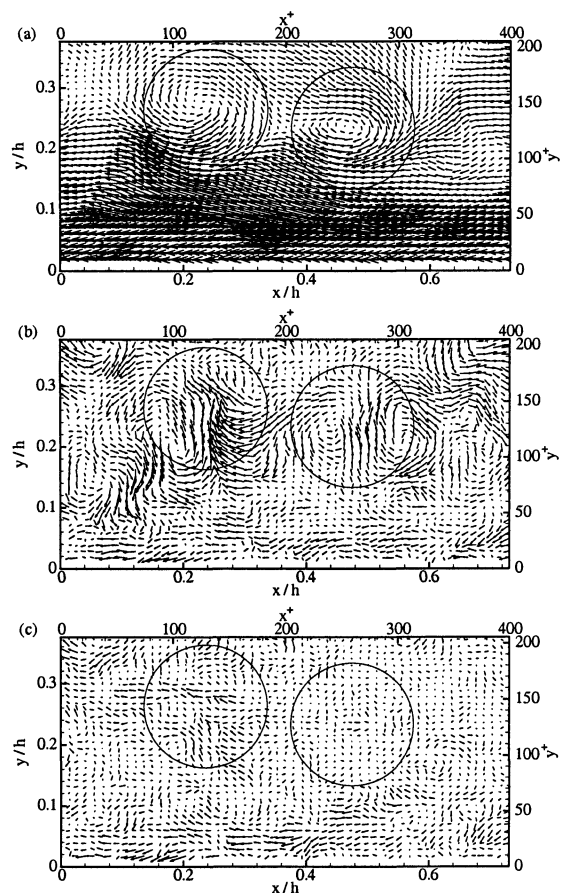

Figure 2: Example of instantaneous velocity and acceleration behavior at $Re_\tau = 547$. (a) Velocity field in reference frame moving with visualized vortices; (b) Instantaneous $\partial u_i/\partial t$ field; (c) Instantaneous $D_b u_i/Dt$ field. Representative spanwise vortex cores are circled to indicate their approximate spatial extent.

(Figure 2(c)), indicating that this pattern is predominantly associated with advection of the small-scale vortices. The bulk convective derivative of velocity is computed in a frame moving at the bulk velocity (U_b)

$$\frac{D_b u_i}{Dt} \equiv \frac{\partial u_i}{\partial t} + U_b \frac{\partial u_i}{\partial x_j}$$
$$\approx \frac{u_i^{C2}(\mathbf{x} + \mathbf{x_c}, t + \tau) - u_i^{C1}(\mathbf{x}, t)}{\tau}, \quad (5)$$

where $\mathbf{x_c} = U_b \tau \mathbf{i}$ and

$$U_b = \frac{1}{2h} \int_0^{2h} U(y) \mathrm{d}y. \quad (6)$$

represents the bulk velocity, the average streamwise velocity over the height of the channel. The time-derivative and bulk convective-derivative fields are shown with the same vector scaling, illustrating that the bulk convective derivative is nearly an order of magnitude smaller than the temporal derivative. In contrast to the signature in the time-derivative

field, the vortices appear to be decelerating slightly in the bulk advective frame. This deceleration is understandable since the induction of the vortices drives them in a direction opposite to the mean flow (i.e. upstream against the mean flow). The deceleration is especially large above and to the right of the vortex center. In the reference frame of the vortex, higher-speed fluid from the outer flow is being swept toward the wall by the induction of the vortex, and its motion is impeded by the presence of lower-speed fluid, hence producing a net deceleration.

Figure 3 contains a sample velocity field, along with the associated velocity rate of change and bulk convective-derivative fields, at $\mathrm{Re}_\tau = 1734$. Three vortices are present in the field of view and each of these vortices produces a strong mushroom-shaped acceleration event in the time-derivative field similar to that seen at $\mathrm{Re}_\tau = 547$. As was noted for the lower Reynolds number, the convective-derivative pattern associated with the instantaneous spanwise vortices is a marked deceleration in a frame of reference moving with the vortices. In addition, with increasing Reynolds number, the velocity time-derivative signature appears to diminish slightly in coherence, while the magnitude of the bulk convective derivative increases slightly with Reynolds number. This trend indicates that evolution effects increase while advective effects decrease with Reynolds number.

'AVERAGE' TEMPORAL AND CONVECTIVE DERIVATIVE BEHAVIOR

From the examples presented in Figures 2 and 3, there appears to be a consistent temporal- and convective-derivative pattern associated with the spanwise vortices embedded within the flow. The "average" character of these patterns can be studied by considering the conditional average of $\partial u_i/\partial t$ and $D_b u_i/Dt$ given the presence of a vortex core (A similar procedure was introduced by Christensen and Adrian (2001) to study the average behavior of velocity given the presence of a single vortex core in turbulent channel flow). These conditional averages take the form

$$\left\langle \frac{\partial u_j}{\partial t}(\mathbf{x}') \middle| \lambda_{ci}(\mathbf{x}) \right\rangle \qquad (7)$$

and

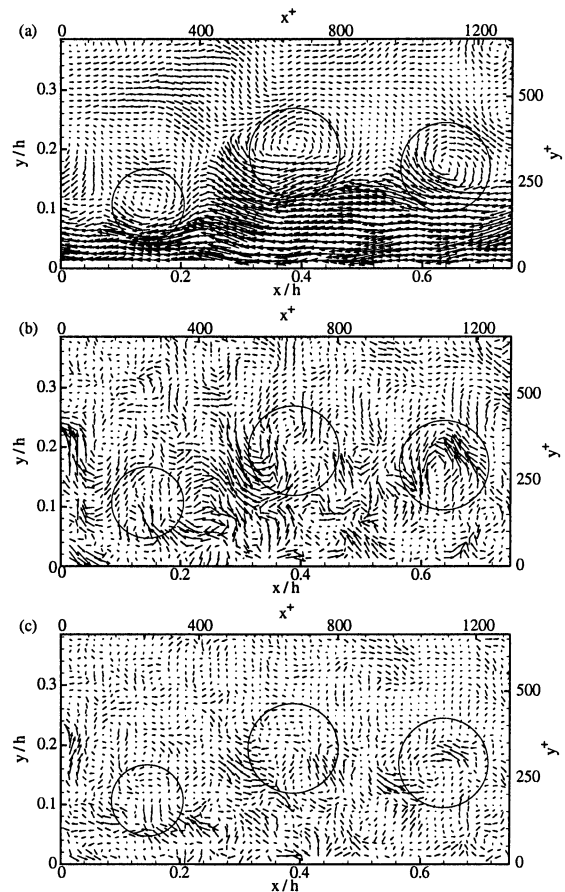$$\left\langle \frac{D_b u_j}{Dt}(\mathbf{x}') \middle| \lambda_{ci}(\mathbf{x}) \right\rangle, \qquad (8)$$

Figure 3: As Figure 2, but $\mathrm{Re}_\tau = 1734$.

where λ_{ci} is a vortex identifier called swirling strength (i is not an index in this definition, but an abbreviation for the word "imaginary"). Swirling strength is the imaginary portion of the complex eigenvalue of the local velocity gradient tensor; it is an unambiguous measure of rotation (Zhou et al., 1999). Unlike vorticity, swirling strength does not highlight regions of intense shear, and it has been shown to be an effective identifier of true vortex cores. Since complex eigenvalues of the velocity gradient tensor occur in conjugate pairs, the positive imaginary part is assigned to λ_{ci}. Therefore, by convention, $\lambda_{ci} \geq 0 \; \forall \; \mathbf{x}$.

Direct computation of the conditional averages postulated above is impractical, so they must be estimated in some fashion. Stochastic estimation of conditional averages minimizes the error between the conditional average and the estimate in a mean-square sense (Adrian, 1988) (the reader is directed to this reference for a comprehensive discussion of stochastic estimation). Studies of many types of turbulent fields have shown that linear estimates are surprisingly accurate and relatively simple to form (Adrian et al., 1987). Therefore, the conditional average presented in (7), for example,

can be estimated in a linear fashion as

$$\left\langle \frac{\partial u_j}{\partial t}(\mathbf{x}') \middle| \lambda_{ci}(\mathbf{x}) \right\rangle \approx L_j \lambda_{ci}(\mathbf{x}), \qquad (9)$$

where the kernel L_j is determined by minimizing the mean-square-error between the estimate and the conditional average. This error minimization gives

$$\left\langle \frac{\partial u_j}{\partial t}(\mathbf{x}') \middle| \lambda_{ci}(\mathbf{x}) \right\rangle \approx \frac{\langle \lambda_{ci}(\mathbf{x}) \frac{\partial u_j}{\partial t}(\mathbf{x}') \rangle}{\langle \lambda_{ci}(\mathbf{x}) \lambda_{ci}(\mathbf{x}) \rangle} \lambda_{ci}(\mathbf{x}).$$
$$(10)$$

(In a similar manner, the conditionally averaged bulk-convective-derivative can be estimated by replacing $\partial u_i/\partial t$ with $D_b u_i/Dt$ in (10)).

From (10), it is clear that the estimate of the conditional average is only a function of unconditional two-point correlations. Therefore, (10) allows one to reconstruct the average velocity time-derivative behavior associated with any given value of λ_{ci} at $\mathbf{x}$. However, it is important to note that since the event in the conditional average is simply a single scalar value, it is sufficient to specify $\lambda_{ci} > 0$ (a non-trivial event). That is, the magnitude of the velocity time-derivative within a given estimate is simply amplified or attenuated by the chosen value of λ_{ci}. Therefore, since thresholding of λ_{ci} is not necessary, the estimate remains objective beyond the choice of event type and event location in the wall-normal direction.

For reference, the estimate of the conditionally averaged velocity field given the presence of a vortex core computed by Christensen and Adrian (2001) is shown in Figure 4(a) at $Re_\tau = 547$. The average vortex pattern shown in this figure is consistent with the spanwise vortex cores visible in the instantaneous velocity realization presented in Figure 2(a): circular cross-section, clockwise rotation, and induction of low-speed fluid away from the wall (a Q_2 event in the nomenclature of Wallace et al. (1972)).

Figure 4(b) illustrates the estimate of the conditionally averaged velocity time-derivative field given the presence of the vortex core at $Re_\tau = 547$ (The conditionally averaged results at $Re_\tau = 1734$ are qualitatively identical to those at $Re_\tau = 1734$, but, due to space limitations, are not shown). Near the center of the vortex there exists a strong wall-normal acceleration away from the wall, coupled with a weak deceleration in the streamwise direction. Additionally, a roll-up in the acceleration exists both upstream and downstream of the
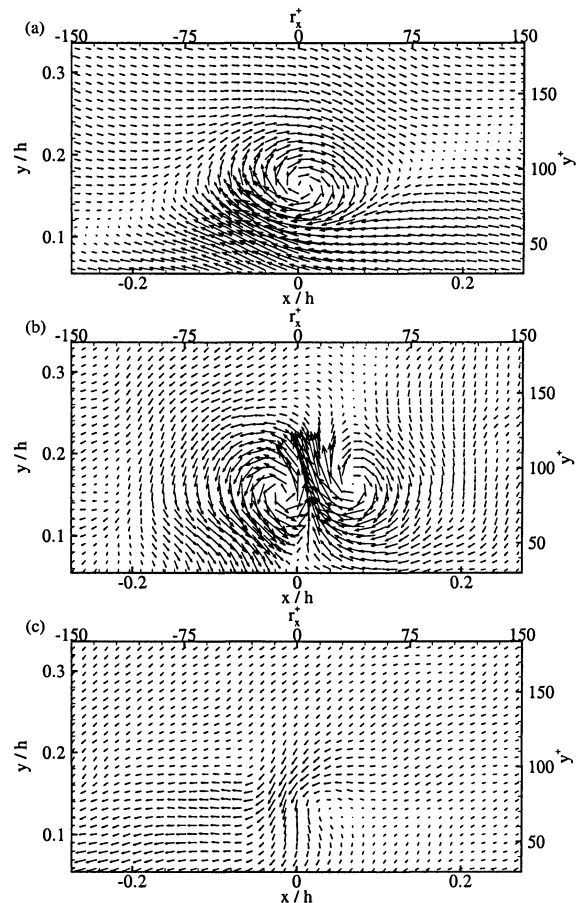

Figure 4: Linear stochastic estimation of u_i, $\partial u_i/\partial t$, and $D_b u_i/Dt$ given the presence of a vortex core at $Re_\tau = 547$ for $y_{ref}/h = 0.15$. (a) Estimate of conditionally averaged velocity; (b) Estimate of conditionally averaged $\partial u_i/\partial t$; (c) Estimate of conditionally averaged $D_b u_i/Dt$.

vortex center. This average pattern is quite similar to the instantaneous patterns seen in Figures 2(b) and defines a consistent velocity time-derivative signature associated with the spanwise vortex cores. In addition to the dominant small-scale event near the vortex center, a larger-scale, relatively uniform deceleration exists further away from the wall.

Figure 4(c) illustrates the estimate of the conditionally averaged bulk convective derivative given the presence of a vortex core at $Re_\tau = 547$. The mushroom-like pattern that is so dominant in the time-derivative field (Figure 4(b)) is noticeably absent in the bulk convective-derivative field. Additionally, the estimate of the conditionally averaged bulk convective derivative contains a marked deceleration in both the streamwise and wall-normal directions above the vortex center, quite similar to the deceleration noted in the instantaneous field presented in Figure 2(c). However, the most striking feature of the bulk convective-derivative field is the large-scale, relatively uniform deceleration in both spatial
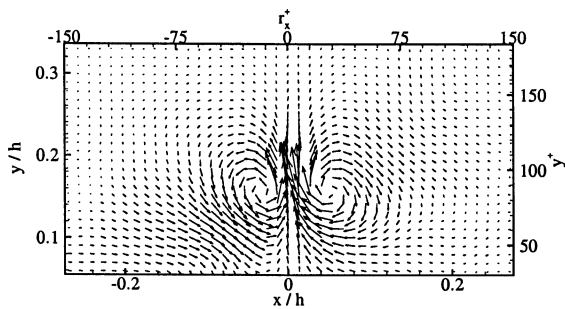
Figure 5: Time-derivative pattern associated with numerical advection of the vortex core shown in Figure 4(a). The average vortex is numerically "advected" one gridpoint in the streamwise direction in the spirit of Taylor's frozen field hypothesis and numerically differenced with the original average vortex to yield a simulated $\partial u_i / \partial t$ field.

directions. This weak deceleration is also evident away from the vortex location in the stochastically estimated $\partial u_i / \partial t$ field; however, its strength is quite small compared to the small-scale advective signature of the vortices. This large-scale deceleration is the imprint of the flow evolution and may be due to the influence exerted by larger, older, and faster vortex packets on smaller, younger, and slower packets closer to the wall.

The advection pattern of the spanwise vortices embedded within the flow can be isolated from the true accelerations using Taylor's hypothesis. The velocity-vector pattern shown in Figure 4(a) was "advected" in the streamwise direction by a single gridpoint to simulate the advection of the vortex downstream. The difference between the "advected" vortex and the original pattern was computed, yielding a simulated velocity time-derivative field in a fixed reference frame (Figure 5). The qualitative pattern of this velocity time derivative is exactly the mushroom-like pattern noted in the instantaneous and average velocity time-derivative fields. Therefore, the mushroom-like patterns seen in the instantaneous and average velocity time-derivative fields are associated predominantly with advection, while the weaker, large-scale deceleration is associated with the evolution of the flow.

SUMMARY

The hairpin/hairpin-like vortices and larger-scale vortex packets present in wall turbulence create clear patterns in both $\partial u_i / \partial t$ and $D_b u_i / Dt$. The advection pattern of the small-scale vortices consists of a mushroom-like shape, with a strong wall-normal deceleration coincident with the vortex center. This behavior indicates that $\partial u_i / \partial t$ is highly intermittent since it is predominantly associated with

smaller scales of the flow. In contrast, the evolution appears to be associated predominantly with larger spatial scales. The marked large-scale deceleration noted in the stochastically estimated bulk convective derivative can be explained by the passage of larger, older, and faster vortex packets past smaller, younger, and slower packets closer to the wall.

REFERENCES

R. J. Adrian. Linking correlations and structure: Stochastic estimation and conditional averaging. In *Zoran P. Zaric Memorial International Seminar on Near-Wall Turbulence*, Dubrovnik, Yugoslavia, 1988. Hemisphere.

R. J. Adrian and W. L. Earley. Evaluation of laser-Doppler velocimeter performance using Mie scattering theory. Technical Report 479, Department of Theoretical and Applied Mechanics, University of Illinois at Urbana-Champaign, 1976.

R. J. Adrian, C. D. Meinhart, and C. D. Tomkins. Vortex organization in the outer region of the turbulent boundary layer. *J. Fluid Mech.*, 422:1–54, 2000.

R. J. Adrian, P. Moin, and R. D. Moser. Stochastic estimation of conditional eddies in turbulent channel flow. In *CTR Proc. of the Summer Program*, pages 7–19, 1987.

K. T. Christensen and R. J. Adrian. Statistical evidence of hairpin vortex packets in wall turbulence. *J. Fluid Mech.*, 431:433–443, 2001.

R. J. Hill and S. T. Thoroddsen. Experimental evaluation of acceleration correlations for locally isotropic turbulence. *Phys. Rev. E*, 55 (2):1600–1606, 1997.

M. Pinsky, A. Khain, and A. Tsinober. Accelerations in isotropic and homogeneous turbulence and taylor's hypothesis. *Phys. Fluids*, 12(12):3195–3204, 2000.

J. M. Wallace, H. Eckelmann, and R. S. Brodkey. The wall region in turbulent shear flow. *J. Fluid Mech.*, 54:39–48, 1972.

P. K. Yueng. One- and two-dimensional lagrangian acceleration correlations in numerically simulated homogeneous turbulence. *Phys. Fluids*, 9(10):2981–2990, 1997.

J. Zhou, R. J. Adrian, S. Balachandar, and T. M. Kendall. Mechanisms for generating coherent packets of hairpin vortices in channel flow. *J. Fluid Mech.*, 387:353–396, 1999.